Journal of Materials Chemistry C

# Microfluidic Thermal Flow Sensor Based on Phase-Change Material with Ultra-High Thermal Sensitivity

| | |
|---|---|
| Journal: | *Journal of Materials Chemistry C* |
| Manuscript ID | TC-ART-09-2022-004047.R1 |
| Article Type: | Paper |
| Date Submitted by the Author: | 23-Nov-2022 |
| Complete List of Authors: | Cao, Yunqi Cao; Zhejiang University<br>Wang, Tongyu; NVIDIA Corp<br>Sepulveda, Nelson; Michigan State University, Electrical and Computer Engineering |
| | |

SCHOLARONE™
Manuscripts

Journal Name

ARTICLE TYPE

Cite this: DOI: 10.1039/xxxxxxxxxx

# Microfluidic Thermal Flow Sensor Based on Phase-Change Material with Ultra-High Thermal Sensitivity

Yunqi Cao[a], Tongyu Wang[b], and Nelson Sepúlveda[b]

Received Date
Accepted Date

DOI: 10.1039/xxxxxxxxxx

www.rsc.org/journalname

A microfluidic thermal mass flow sensor based on planar micro-machining technology and a phase-change material is designed, fabricated, and characterized. The sensor configuration uses a small patch of vanadium dioxide ($VO_2$) thin film as the sensing element closely placed in the down streaming direction of the heat source. By operating the $VO_2$ sensor in the phase transition region, no thermal insulation structure is required due to the ultra-high thermal sensitivity in this region. The characteristic 3-order resistance change, from 290 kΩ to 290 Ω, is observed during the full heating and cooling cycles by using both substrate heating and resistive heating methods. The equivalent maximum temperature coefficient of resistance (TCR) is calculated to be -0.37 $K^{-1}$ in the cooling cycle and -0.43 $K^{-1}$ in the cooling and heating cycle, respectively. The sensing operation principle is determined to follow the major cooling curve to avoid falling into minor loops and to secure high TCR. The resistance of $VO_2$ is monitored under flow rates ranging from 0 to 37.8 $\mu L \cdot s^{-1}$ with the maximum sensitivity of 1.383%/($\mu L \cdot min^{-1}$). The studies presented in this research may enable the application of utilizing nonlinear metamaterial in microfluidic flow sensors with orders of magnitude improvement in sensitivity.
*e.g.* [Surname *et al., Journal Title*, 2000, **35**, 3523].

## 1 Introduction

Microfluidic flow sensors based on microelectromechanical systems (MEMS) technology have been widely implemented in numerous applications such as chromatography, flow cytometry, and particle counting/sorting, etc. By integrating such components into microfluidic devices or micro total analysis systems ($\mu$TAS), the detection can be realized with portability, low sample consumption, high precision, and rapid response. Among all sensing mechanisms, thermal flow sensors have drawn largest interests due to their high sensitivity and accuracy, low signal drift, and simple implementation. The measurement of the fluid flow rate is achieved by evaluating the heat dissipation that is transduced into electrical signals. Typical configurations include anemometric, calorimetric, and time-of-flight sensors[1]. For commonly used thermal flow sensor materials such as Pt and Ni[2], the temperature coefficient of resistance (TCR) is typically in the range of 7000 ppm$\cdot K^{-1}$. Strategies of increasing sensitivity mainly focus on maximizing heat transfer from the heating element to the sensing element through fluid transportation. MEMS bulk machining process is often introduced to construct thermal isolation cavity[3] or clamped-clamped beam structure with heating and sensing element individually suspended in the fluid[4], which limits the heat conduction loss through the substrate and hence improves the sensing performance. However, this inevitably induces extra fabrication and packaging difficulties and reduces the robustness of the device[5]. Thus, it is worth exploring new thermo-resistive materials with higher TCRs that may effectively resolve the above trade-off.

In order to improve the sensitivity of thermal flow sensors, consecutive efforts in materials science and nanotechnologies have been made to increase the TCR of non-metal thermal-sensitive materials. With vacuum thermal annealing and electrical aging treatment, both electrical stability and thermal sensitivity of single-walled carbon nanotube (SWCNT) can be significantly improved[6], leading to a high TCR of 8040 ppm$\cdot K^{-1}$. In addition, structures of nanowires (NWs) are often used to increase the thermal sensitivity for small temperature fluctuation monitoring[7]. By subsequently implementing focused ion beam (FIB), wet etching, and annealing processes[8], silicon NWs (SiNWs) has demonstrated a high negative TCR of -12000 ppm$\cdot K^{-1}$. Recently, cubic silicon carbide (3C-SiC) has been introduced for air flow sensing at elevated temperatures[9,10], the TCR is found to be -20720 ppm$\cdot K^{-1}$ at ambient temperature and -9287 ppm$\cdot K^{-1}$ at 200 °C, which is about one order of magnitude higher than Au. These advances in high TCR materials successfully eliminate the

[a] State Key Laboratory of Industrial Control Technology, College of Control Science and Engineering, Zhejiang University, Hangzhou, Zhejiang 310027, China; E-mail: caoyunqi@zju.edu.cn.
[b] Department of Electrical and Computer Engineering, Michigan State University, East Lansing, MI 48824, USA; E-mail: sepulve6@msu.edu.

This journal is © The Royal Society of Chemistry [year]

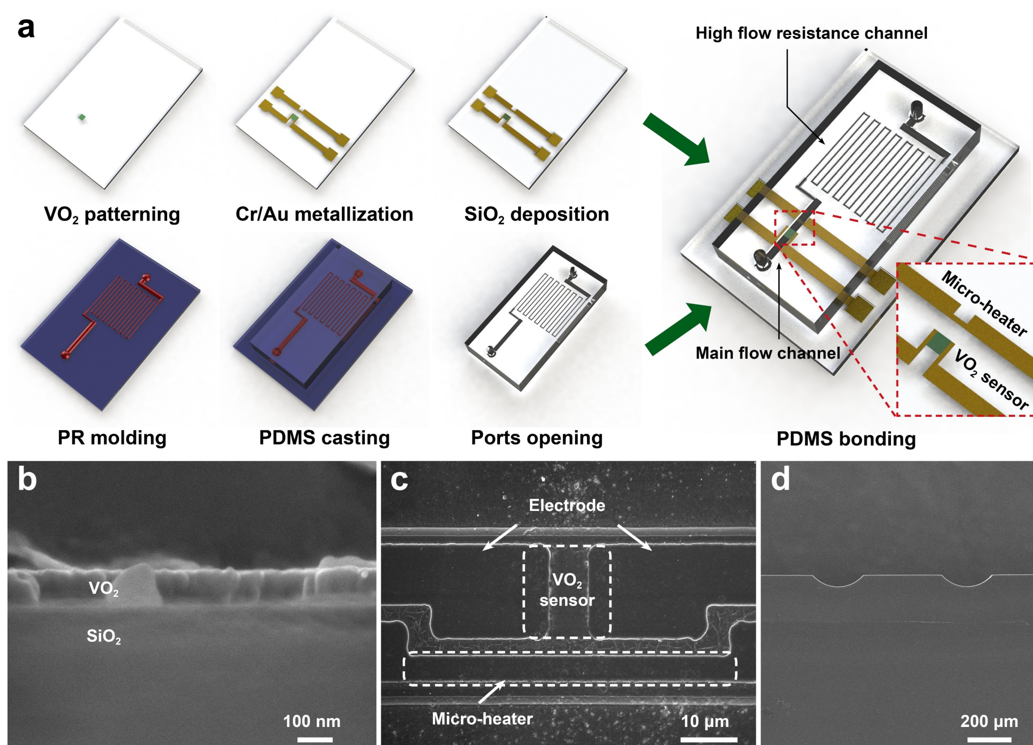


**Fig. 1** $VO_2$-based microfluidic gas flow sensor. (a) Schematic drawing of fabrication process. The sensor layer and flow layer are fabricated individually and bonded together using surface plasma treatment. The inset shows a close-up view of the $VO_2$ sensor and the micro-heater. (b) Cross-section view SEM image of $VO_2$ thin film on $SiO_2$ substrate. (c) Top view SEM image of $VO_2$ sensor, sensing electrodes, and micro-heater. (d) Cross-section view SEM image of PDMS-based microfludic channels.

use of suspended structures while maintaining the high sensitivity. However, the use of phase-change materials with equivalent TCR values showing more than orders of magnitude change across a temperature window of $\sim$ 10 °C presents a potential alternative that has not been investigated until now. Vanadium dioxide ($VO_2$) is a first-order solid-to-solid phase-change material, which undergoes a fully reversible hysteretic insulator-to-metal transition (IMT) starting at ~60 °C[11]. Thermal actuation methods such as conductive heating[12], resistive heating[13], and photothermal irradiation[14,15] are often used to induce the IMT. During phase-change, the electrical resistance shows orders-of-magnitude change in a temperature span of 5 to 15 °C[16]. This abrupt and large change in resistance has enabled the use of $VO_2$ in various applications such as Mott field-effect transistors (FETs) for enhanced electronic transport modulation[17], resistive switches[18–20], smart windows[21], and active memristors for neuromorphic computing[22,23], etc. However, its ultra-high TCR has not yet been implemented in thermal flow microfluidic sensors.

In this study, a fully integrated $VO_2$-based microfabricated thermal flow sensor with enhanced device robustness and simplified fabrication process has been developed to detect gas flow rate in the microliter range. The on-surface thermal sensitive $VO_2$ thin film was successfully synthesized by pulsed laser deposition (PLD), which exhibits a fully reversible hysteretic 3-order magnitude change in resistance during the IMT region under both substrate heating and resistive heating methods. Based on the hysteretic behavior, minor cycles are obtained inside the major heating and cooling loop to investigate the optimum working condition with $VO_2$ maintained at high TCR of -0.37 $K^{-1}$. Finite element method (FEM) study was performed to evaluate the average temperature deviation of the $VO_2$ sensor subjected to forced convection flow, the small temperature change limited by the substrate induced conduction loss can be effectively detected and translated to a notable resistance change due to the high TCR of the sensing material. The proposed sensing technology provides useful information for researchrs trying to increase sensitivity of microfluidic thermal flow sensors by using phase-change materials.

## 2 Materials and Methods

### 2.1 Synthesis of $VO_2$ thin film

A $VO_2$ thin film of 100 nm thickness was synthesised and deposited by the PLD method on a 2-inch $SiO_2$ wafer, which was performed in a vacuum chamber with base vacuum level below 0.01 mTorr and $O_2$ atmosphere of 15 mTorr. During the deposition, the wafer was heated from the backside by radiation, where a ceramic heater was placed at a distance of 1 inch and maintained at 595 °C. The excimer laser pulses with the energy of 356 mJ and repetition rate of 20 Hz were ablated onto the vanadium target which is located 1.75 inches in front of the $SiO_2$ wafer for 25 min. After the deposition, a 30 min annealing process was followed with the same deposition condition. Depending on the application, $VO_2$ thin films can be modified to have lower transition temperatures (achieved by, for example, growing pre-stressed $VO_2$ thin films


This journal is © The Royal Society of Chemistry [year]

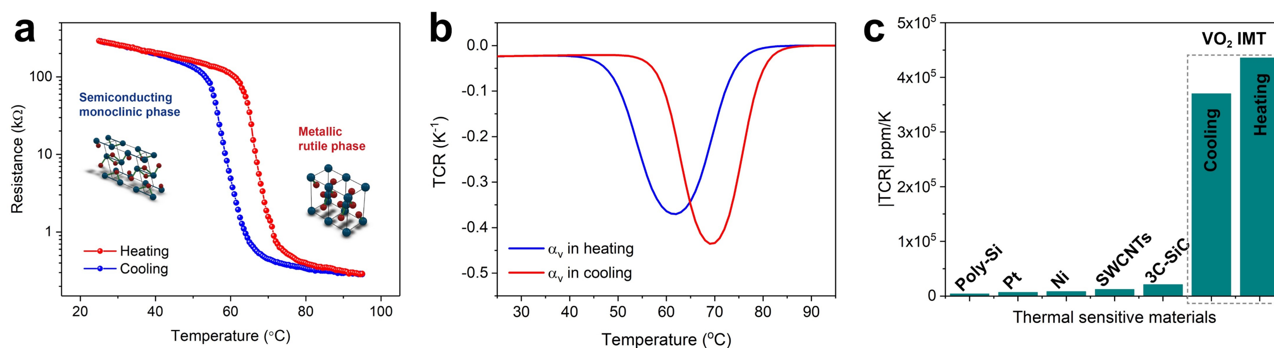


**Fig. 2** Thermal-electrical properties of $VO_2$. (a) Experimentally measured resistance of the $VO_2$ sensor as a function of temperature during the fully reversible heating and cooling cycle using substrate heating. (b) Temperature-dependent TCR value of $VO_2$ in the major heating and cooling curves across the phase-change region. (c) Comparison of TCR values of $VO_2$ in different temperature regions with various commonly used thermal sensitive materials.

on certain substrates[24], or reducing crystallite size to lower hysteresis and the abruptness of the phase transition[25]. The $VO_2$ deposition process used in this work is aimed to increasing the magnitude of the changes across the phase transition. In order to confirm the quality of the $VO_2$ thin film, the film resistance was measured as a function of temperature in the full heating and cooling cycle between 25 °C and 95 °C. The measurement shows a more than 3 orders of magnitude change in resistance during the IMT region, indicating a good film quality.

### 2.2 Integration of $VO_2$-based thermal flow sensor

The thermal flow sensor used in this work consists of two main components, which include a $VO_2$-based thermal sensing layer and a PDMS-based fluidic layer individually fabricated and integrated by the plasma bonding process as schematically demonstrated in Fig. 1a. After the $VO_2$ film deposition, the $VO_2$ thermal sensor was patterned by the reactive ion etching (RIE). In the next step, metal traces that are used for measuring $VO_2$ resistance and applying resistive heating current were both deposited and patterned simultaneously. This was done by sequentially depositing a 20 nm Cr thin film and a 200 nm Au thin film using a metal sputtering system, where the Cr layer was used to increase the adhesion strength of the metal traces. Then, the micro-heater and the electrodes were patterned by the lift-off method. As shown in Fig. 1c, the micro-heater is narrower than the electrodes and has a higher resistance. Therefore, the generated is concentrated in this small area, creating a localized heating effect. After that, a 1 $\mu$m $SiO_2$ passive layer was also deposited by using plasma-enhanced chemical vapor deposition (PECVD) at a temperature of 250 °C on top to protect the $VO_2$ sensor from the following RIE process. The device protection by the $SiO_2$ layer also allows the flow rate measurement of other liquid fluids, such as water, alcohol, and oil, showing expandability to other applications. Openings were also created on the $SiO_2$ passive layer by RIE for the wire bonding purpose to complete the fabrication of the thermal sensing layer. Fig. 1b and Fig. 1c show the cross-sectional and top scanning electron microscopy (SEM) view images of the $VO_2$ thin film on a $SiO_2$ substrate and the sensor-heater pair, respectively.

The fabrication of the fluidic layer was realized by the standard procedures of soft lithography and replica molding techniques. To begin with, a photoresist (AZ9260, MicroChemicals, GmbH.) mold was constructed by using the double spin coating method followed by the photolithographic patterning technique. A thin layer of Hexamethyldisilazane (HMDS) was spin coated on top of the Si wafer for 60 sec at the spin rate of 2000 rpm. The wafer was then baked at 100 °C for 30 sec to evaporate excess solvent. The first photoresist (PR) layer was spin coated for 60 sec at 1000 rpm. After 90 seconds, the second PR layer was also spun coated by the same method as the first layer. A 5 min soft bake process was performed at 90 °C in order to reduce the residual solvent concentration. The wafer was then placed underneath the shadow mask and exposed to the UV light for 90 sec with the intensity of 10 $mW/cm^2$. The pattern of flow channels were developed by the 1:2 AZ400K (MicroChem Corp.) developer solution. After the wafer was cleaned and air dried, a thermal reflow process was carried out at 120 °C for 15 min to develop a round structure border of the flow channel to ensure the laminar flow. After the PR mold is constructed, a silanization process by 3-aminopropyltriethoxysilane was performed before the casting in order to facilitate the PDMS peeling-off of the mold. The polymer solution was prepared by PDMS (184 Silicone Elastomer, Dow Corning Corp.) with a prepolymer/curing agent weight ratio of 10:1. The uncured solution was poured onto the PR mold and placed in a vacuum desiccator for a 60 min degassing. When the solution was thermally polymerized, the PDMS fluidic layer was peeled off with the help of blade and the ports for fluid inlet and outlet were created by using a luer stub. The fabricated fluidic layer has a total thickness of 3 mm with an embedded microfluidic channel of 54 $\mu$m in height as shown in Fig. 1d. Next, $O_2$ plasma treatment was applied on both $SiO_2$ and PDMS surfaces for 20 sec in order to bond the thermal sensing layer with the fluidic layer. The bonding process is performed under an optical microscope with the help of the alignment mark on the $SiO_2$ substrate to ensure the $VO_2$ sensor is located in the middle of the main flow channel. Finally, the device was subsequently baked at 140 °C on a hotplate for 40 min to increase the bonding strength.

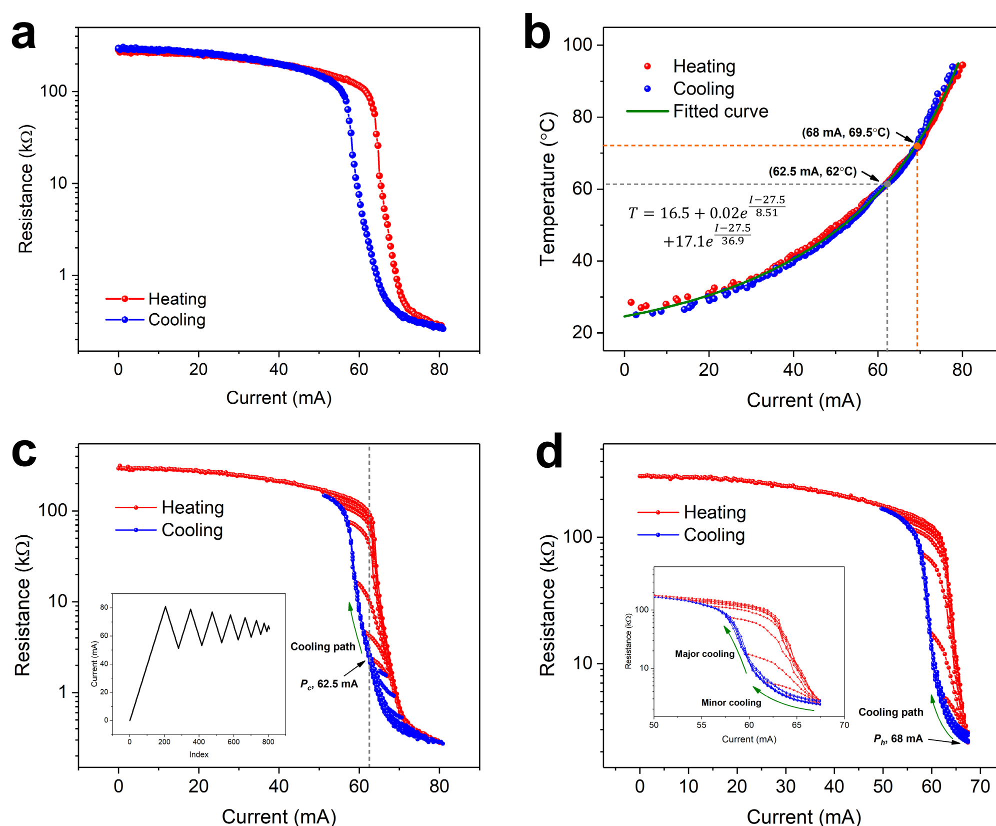


**Fig. 3** Evaluation of the optimal operating condition in the proposed $VO_2$-based microfluidic thermal flow sensor. (a) Resistance of the $VO_2$ sensor as a function of current during the fully reversible heating and cooling cycle using resistive heating. (b) Correlation between the $VO_2$ sensor temperature and the resistive heating current supplied to the micro-heater, where the critical current values related to the temperatures with optimal TCR are indicated. (c) Major hysteresis loop with different minor loops by cooling from different preheating currents, the inset shows the sequence of applied currents. (d) Resistance change falls into the minor loop by cooling from the major heating curve in the phase-change region, the inset shows a zoomed-in view of minor loops.

## 3 Results

Fig. 2a shows the 3-order, hysteretic resistance change of the $VO_2$ films used in this work during the full heating and cooling cycle, due to the thermal-induced phase transition between low-temperature semiconducting monoclinic phase and high-temperature metallic rutile phase. The precise control of the substrate temperature is realized by using a closed-loop temperature control system demonstrated in our previous work[12]. The temperature-dependent resistance $\rho(T)$ in the major heating curve starts a sharp decrease at around 62 °C and spans about 15 °C until the $VO_2$ micro-crystals are fully transformed into rutile phase. From the measured resistance curve, the temperature-dependent TCR of $VO_2$ ($\alpha_v(T)$) can be determined as $\alpha_v(T) = \rho(T)[d\rho(T)/dT]$, for both heating and cooling curves as a function of temperature, which is shown in Fig. 2b. It can be seen that the maximum value of $\alpha_v(T)$ in the heating and cooling curves occurs at different temperatures due to the hysteretic behavior, which is calculated to be -0.43 $K^{-1}$ at 69.5 °C and -0.37 $K^{-1}$ at 62 °C, respectively. Fig. 2c shows the comparison of TCR values for $VO_2$ and other temperature-sensitive materials, where the maximum $\alpha_v(T)$ in the IMT region shows values more than 60 times higher than conventional metallic thermal sensing materials, such as Pt[2], which is the material used as the sensing element in most microfluidic thermal flow sensors. It should be noted that although the ultra-high $\alpha_v(T)$ can only be obtained in a small temperature window, the room temperature $\alpha_v(T)$ still maintains at a high value of -0.024 $K^{-1}$, which is comparable to the recently proposed cubic silicon carbide (3C-SiC)[10] and single-walled carbon nanotubes (SWCNTs)[6], and still 6 times higher than Pt.

Before analyzing the results of the proposed $VO_2$-based thermal flow sensor, it is important to explain its working principle and operation for this particular application. As shown in Fig. 2b, the maximum TCR occurs at elevated temperatures in both heating and cooling curves, indicating the requirement of preheating the $VO_2$ sensor. On this basis, resistive heating is used to locally heat the $VO_2$ sensor with minimized heat loss by applying DC current into a fully integrated micro-heater that is closely located in the upstream direction of the sensor. Fig. 3a shows the resistance change in the $VO_2$ sensor throughout the IMT region as a function of resistive heating current. The curve shows a 3-order resistance change from ~290 to ~0.29 kΩ by applying an 80 mA current cycle. Although this sensor configuration reduces the complexity of the fabrication process due to the simultaneously patterning of the micro-heater and the sensing electrodes, the temperature difference in the micro-heater and the $VO_2$ sensor requires an


This journal is © The Royal Society of Chemistry [year]

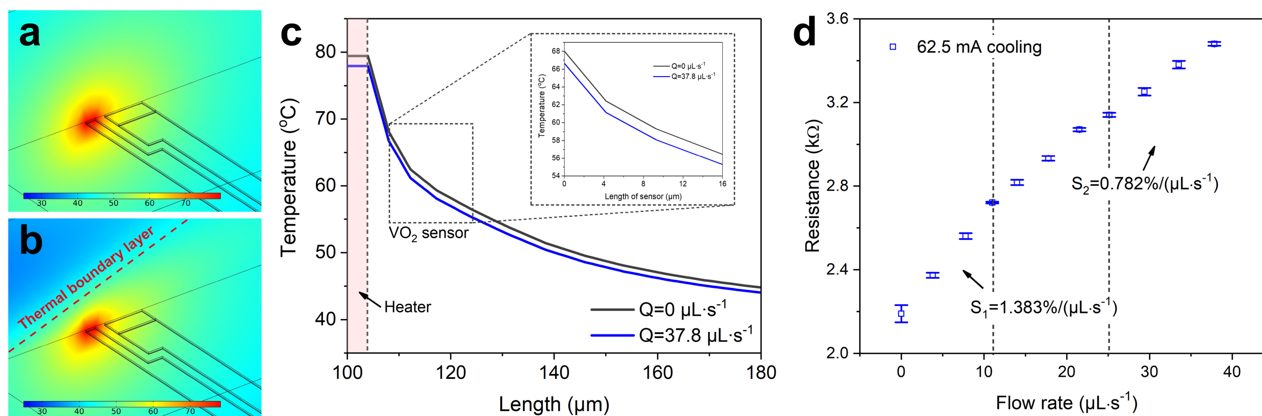


**Fig. 4** FEM simulation and experimental results of $VO_2$-based microfluidic thermal flow sensor. Temperature distribution around the micro-heater (a) with no gas flow and (b) under a flow rate of 37.8 $\mu$L·s$^{-1}$, where the thermal boundary layer is formed. (c) The change of temperature distribution along the channel direction upon cooling from the preheating point $P_c$, the inset shows the temperature change in the $VO_2$ sensor. (d) Experimental measurement of $VO_2$ resistance as a function of flow rate under convective flow.

additional interpolation of the sensor temperature in order to determine the optimal operating condition with the maximum TCR in terms of resistive heating current. By comparing Fig. 2a and Fig. 3a, the temperature of the $VO_2$ sensor can be determined as a function of current by correlating the resistive heating current with the substrate heating temperature using the $VO_2$ sensor resistance in both major heating and cooling curves as shown in Fig. 3b. It should be noted that the hysteretic behavior only exists in the temperature-dependent electrical properties (e.g. resistance and TCR) of the $VO_2$ sensor, thus the sensor temperature ($T$) in both heating and cooling curves increases monotonically with heating current ($I$) and can be fitted with the same exponential function. Therefore, the optimal working temperatures that show the maximum TCR of -0.43 K$^{-1}$ and -0.37 K$^{-1}$ in the major heating and cooling curves can be obtained by applying resistive heating currents of 68 mA and 62.5 mA, respectively.

Fig. 3c shows the hysteretic behavior of both the major and the minor loops for the $VO_2$ sensor under resistive heating, where the inset shows the sequence of currents to generate minor loops. For thermal flow sensing applications, the decrease in the sensor temperature due to convection loss would cause the resistance change to follow minor cooling curves with lower TCR due to smaller slopes. As further illustrated in Fig. 3d, although the sensor resistance would eventually enter the major cooling curve with higher TCR after the sensor temperature is decreased for more than ∼5 °C, the sensitivity in the low flow rate range is still significantly limited. Thus, when the sensor is operated at point $P_h$ with a pre-heating current of 68 mA in the major heating curve as shown in Fig. 3d, the actual TCR is much lower than the theoretical value of -0.43 K$^{-1}$ as demonstrated in Fig. 2b. Nevertheless, the maximum TCR of -0.37 K$^{-1}$ in the major cooling curve can be achieved when $P_c$ of 62.5 mA is selected as the operation point as shown in Fig. 3c. It is also worth noting that the optimal operation current may vary depending on the ambient environment temperature due to the ultra-high thermal sensitivity of $VO_2$. Thus, it is essential to keep in mind that the maximum TCR value determines this pre-heating current in the cooling loop for the proposed sensing principle.

To evaluate the temperature change in the $VO_2$ sensor under a forced convection flow, a finite element method (FEM) simulation is carried out using COMSOL Multiphysics 5.3. Fig. 4a shows the simulation result of the temperature distribution in the sensing area (around the micro-heater) under a zero flow rate condition by operating at preheating point $P_1$, the thermal profile extends into both the $VO_2$ sensor and the $SiO_2$ substrate due to the heat conduction. The temperature distribution under a flow rate ($Q$) of 37.8 $\mu$L·s$^{-1}$ is also simulated in Fig. 4b, where the temperature distribution changes significantly in the fluid due to the convection loss and a thermal boundary layer is formed. However, the temperature distribution in the $SiO_2$ substrate is barely affected because the thermal conduction is dominated in the heat transfer processes in the substrate, leading to a small temperature decrease in the $VO_2$ sensor. Fig. 4c shows the simulation result of the temperature distribution in the channel direction around the sensing area. It can be seen that the temperature decreases under an air flow rate of 37.8 $\mu$L·s$^{-1}$ across the $VO_2$ sensor, which gives a small average temperature change of about -1.26 °C due to the absence of thermal cavity structure. It is worth mentioning that although additional heat is carried from the micro-heater to the downstream $VO_2$ sensor due to the convective flow, the temperature increase is overridden by the cooling of the upstream micro-heater, which is contrary to the case when a thermal cavity is used[26].

Experimental measurements were also performed to validate the performance of the $VO_2$-based thermal flow sensor. In order to operate around the high TCR, a Joule heating current of 80 mA was first applied to the micro-heater and then decreased to maintain the optimal operation current at point $P_c$ of 62.5 mA in the major cooling curve. Airflow was then forced into the microchannel using a customized pressure-driven microfluidic pump with the inlet pressure in the range of 0 to 100 kPa. The flow rate was determined by using a small segment of deionized water, which has limited impact on the flow rate under the same driven pressure, as the tracer object and measuring the advancing of the

front-edge of the liquid under an optical stereo-microscope. Thus, the flow rate can be estimated based on the velocity of the tracer object and the cross-sectional area of the micro-channel. Fig. 4d shows the resistance of the $VO_2$ sensor as a function of flow rate measured by a source measure unit Keithley 2450, the resistance changes from $\sim$2.2 to 3.5 kΩ in the range of 0 to 37.8 $\mu$L·s$^{-1}$, which translates to a percentage change of $\sim$59%. According to Fig 2a, the resistance change under $Q$ = 37.8 $\mu$L·s$^{-1}$ corresponds to a 1.01 °C decrease in temperature starting from 61.68 to 60.67 °C and is in agreement with the FEM results as shown in Fig. 4c. The TCR in this small temperature range maintains at a high level of -0.37 ± 0.018 K$^{-1}$ and gives a sensitivity of 1.383%/$\mu$L·s$^{-1}$ in the low flow rate range of 0 - 14 $\mu$L·s$^{-1}$ and 0.782%/$\mu$L·s$^{-1}$ in the range above 25 $\mu$L·s$^{-1}$, respectively. In order to investigate the sensing stability, the coefficient of variation (CV, defined as the ratio of the standard deviation to the mean) was calculated to be 1.88% in the initial state. This relatively higher CV can be attributed to the thermal susceptibility to the ambient environment because the heat transfer is mainly caused by heat conduction under the zero flow condition. However, when air flow is forced into the micro-channel, the heat transfer is dominated by convection. In this case, the CV has lower values in the range of 0.15 - 0.55%, demonstrating high sensing stability in air flow rate measurement for the proposed $VO_2$ flow sensor. If Pt was used as the thermal sensor in the same configuration, then the resistance change in the same temperature window would only be $\sim$0.4%, which is more than two orders lower than the sensitivity of the $VO_2$ sensor, and may not be above the noise floor of many instruments. Therefore, the ultra-high TCR of $VO_2$ in the IMT region demonstrates a potential application in thermal flow sensing based on a on-surface sensor structure, which can significantly decrease the fabrication cost and increase the device robustness with acceptable sacrifice in the sensitivity.

## 4 Conclusions

In summary, this work reports a $VO_2$-based microfluidic gas flow sensor with an anemometer configuration. The high sensitivity of the $VO_2$ as the thermal sensitive material is verified by the resistance measurement through the full heating and cooling cycles. Both substrate heating and Joule heating methods are used and the characteristic 3 orders of drop in resistance from $\sim$290 to $\sim$0.29 kΩ is observed in the same range. This was used to estimate the average temperature in the $VO_2$ sensor at each Joule heating current value. To secure the optimal TCR for high performance sensing, the major cooling curve is selected as the operation range in order to avoid the minor loops that have much lower TCR values. The maximum TCR is thus found to be -0.37 °C$^{-1}$ at the preheating current of $\sim$62.5 mA °C in the cooling loop, which relates to an average temperature of $\sim$62 °C in the $VO_2$ sensor. Due to the high sensitivity, no thermal isolation cavity is required and the device robustness is consequently improved. The transportation phenomenon in this planar structure shows a suppressed heat convection and is supported by the FEM simulation. In the given test range of $Q = 0 - 37.8$ $\mu$L·s$^{-1}$, the device under test shows an average TCR of -0.37 °C$^{-1}$ with the sensitivity as high as 1.383%/($\mu$L·s$^{-1}$).

## 5 Acknowledgement

This work was supported in part by the National Natural Science Foundation of China under Grant 62103369 and in part by the Michigan State University Foundation Strategic Partnership under Grant 16-SPG-Full-3236. The authors would also like to thank Dr. Rafmag Cabrera for insightful discussions.

## References

1 C. Cavaniol, W. Cesar, S. Descroix and J.-L. Viovy, *Lab on a Chip*, 2022, **22**, 3603–3617.
2 J. T. Kuo, L. Yu and E. Meng, *Micromachines*, 2012, **3**, 550–573.
3 Y. Ou, F. Qu, G. Wang, M. Nie, Z. Li, W. Ou and C. Xie, *Applied Physics Letters*, 2016, **109**, 023512.
4 W. Xu, X. Wang, R. Wang, J. Xu, Y.-K. Lee *et al.*, *IEEE Transactions on Industrial Electronics*, 2020, **68**, 4468–4476.
5 C.-H. Wu, D. Kang, P.-H. Chen and Y.-C. Tai, *Sensors and Actuators A: Physical*, 2016, **241**, 135–144.
6 W. Gao, B. Ma, J. Luo and J. Deng, *Smart Materials and Structures*, 2019, **28**, 075021.
7 Y. Yang, Y. Zhou, J. M. Wu and Z. L. Wang, *ACS nano*, 2012, **6**, 8456–8461.
8 T. Dinh, H.-P. Phan, T. Kozeki, A. Qamar, T. Fujii, T. Namazu, N.-T. Nguyen and D. V. Dao, *Materials Letters*, 2016, **177**, 80–84.
9 T. Dinh, H.-P. Phan, N. Kashaninejad, T.-K. Nguyen, D. V. Dao and N.-T. Nguyen, *Advanced Materials Interfaces*, 2018, **5**, 1800764.
10 V. Balakrishnan, T. Dinh, T. Nguyen, H.-P. Phan, T.-K. Nguyen, D. V. Dao and N.-T. Nguyen, *Review of Scientific Instruments*, 2019, **90**, 015007.
11 F. Morin, *Physical review letters*, 1959, **3**, 34.
12 Y. Cao, D. Hernández-Escobar, C. Boehlert and N. Sepúlveda, *Journal of Microelectromechanical Systems*, 2020, **29**, 132–134.
13 Y. Cao, D. Torres, T. Wang, X. Tan and N. Sepúlveda, *Smart Materials and Structures*, 2017, **26**, 085032.
14 P. Chen, R. Shi, N. Shen, Z. Zhang, Y. Liang, T. Li, J. Wang, D. Kong, Y. Gan, A. Amini *et al.*, *Advanced Intelligent Systems*, 2020, **2**, 2000051.
15 H. Ji, D. Liu, H. Cheng and C. Zhang, *Journal of Materials Chemistry C*, 2018, **6**, 2424–2429.
16 Y. Cao and N. Sepúlveda, *Advanced Materials Interfaces*, 2019, **6**, 1900887.
17 T. Wei, T. Kanki, M. Chikanari, T. Uemura, T. Sekitani and H. Tanaka, *Scientific reports*, 2017, **7**, 1–7.
18 S. Cheng, M.-H. Lee, X. Li, L. Fratino, F. Tesler, M.-G. Han, J. Del Valle, R. Dynes, M. J. Rozenberg, I. K. Schuller *et al.*, *Proceedings of the National Academy of Sciences*, 2021, **118**, year.
19 A. G. Shabalin, J. Del Valle, N. Hua, M. J. Cherukara, M. V. Holt, I. K. Schuller and O. G. Shpyrko, *Small*, 2020, **16**, 2005439.
20 W. A. Vitale, C. F. Moldovan, M. Tamagnone, A. Paone,


This journal is © The Royal Society of Chemistry [year]

A. Schüler and A. M. Ionescu, *IEEE Electron Device Letters*, 2015, **36**, 972–974.

21 J. Figueroa, Y. Cao, H. Dsouza, J. Pastrana and N. Sepúlveda, *Advanced Materials Technologies*, 2019, **4**, 1800599.

22 W. Yi, K. K. Tsang, S. K. Lam, X. Bai, J. A. Crowell and E. A. Flores, *Nature communications*, 2018, **9**, 1–10.

23 Q. Xia, Y. Qin, P. Qiu, A. Zheng and X. Zhang, *Journal of Materials Chemistry B*, 2022, **10**, 1991–2000.

24 Y. Muraoka and Z. Hiroi, *Applied Physics Letters*, 2002, **80**, 583–585.

25 N. Sepúlveda, A. Rúa and F. E. Fernández, *IEEE Transactions on Nanotechnology*, 2010, **9**, 330–334.

26 M. Dijkstra, M. J. de Boer, J. W. Berenschot, T. S. Lammerink, R. J. Wiegerink and M. Elwenspoek, *Sensors and Actuators A: Physical*, 2008, **143**, 1–6.